# Information-rich localization microscopy through machine learning

Taehwan Kim[1†], Seonah Moon[2†], & Ke Xu[2,3]

[1]*Department of Electrical Engineering and Computer Sciences, University of California, Berkeley, CA 94720*

[2]*Department of Chemistry, University of California, Berkeley, CA 94720*

[3]*Chan Zuckerberg Biohub, San Francisco, CA 94158*

[†]*These authors contributed equally*

**While current single-molecule localization microscopy (SMLM) methods often rely on the target-specific alteration of the point spread function (PSF) to encode the multidimensional contents of single fluorophores, we argue that the details of the PSF in an unmodified microscope already contain rich, multidimensional information. We introduce a data-driven approach in which artificial neural networks (ANNs) are trained to make a direct link between an experimental PSF image and its underlying parameters. To demonstrate this concept in real systems, we decipher in fixed cells both the colors and the axial positions of single molecules in regular SMLM data.**

Originally developed toward the specific goal of superior spatial resolution, single-molecule localization (super-resolution) microscopy (SMLM), including STORM/(F)PALM[1–3] and PAINT[4], has evolved in recent years into a generic tool for sampling diverse biologically relevant information at the nanoscale[5]. For example, when combined with environment-sensitive dyes, intracellular heterogeneity in the local chemical environment can be mapped by concurrently obtaining the spatial positions and emission spectra of millions of single fluorescent molecules[6]. Consequently, the full potential of SMLM is expected to be unleashed through the proper multidimensional analysis of the emission wavelength[5], brightness, dipole orientation[7], as well as the axial (3D) position[8] of single molecules.

To date, to extract information beyond the in-plane location, e.g., the emission wavelength and the axial position, of single emitters, would often oblige the explicit encoding of such high-dimensionality information into the diffraction pattern of single molecules (point spread functions; PSFs) through optical aberrations and alterations[5,8], including astigmatism[9], interference[10], wavelength-dependent splitting[11], dispersion[12], and wave-front modification[13]. The resultant, engineered PSF shape and intensity then help establish best-fit models between experimental observables and fluorophore characteristics. Such approaches, each often optimized for a single parameter of interest, inevitably increase the PSF size and/or necessitate the splitting of fluorescence across different channels, and so often incur complicated optics and compromised performances between different parameters. While recent work[14,15] has studied the PSF design for the simultaneous estimation of color and axial position, added optics and enlarged PSFs are still involved, and proper calibration of such Fourier optics-heavy systems is challenging[16].

We reason that even the simplest PSF obtained from an unmodified microscope is rich in information—in addition to the axial location embedded in the defocused PSF, which has been examined in recent work[17,18], the emission wavelength of a fluorophore also sets the scale of PSF in all three dimensions[19]. Contributions from the two sources are distinct yet subtle, and would be hard to decouple via simple models given the difficulties in fully characterizing all system-specific properties.

We present a data-driven approach in which the relationship between a PSF image, obtained from an unmodified commercial microscope, and the underlying multidimensional characteristics of an emitter is directly established by a supervised machine learning algorithm. A related approach has been recently used in astronomy for stellar classification[20]. Although SMLM faces additional challenges associated with the vast range of axial positions (as opposed to stars always at infinity), it benefits from the ready access to arbitrary amounts of experimental PSFs that may be acquired under identical conditions. By training generic learning models using such datasets, an end-to-end framework from raw PSF images to the molecule characteristics can be constructed.

To demonstrate this concept, we developed a method for machine learning-based 3D multi-color SMLM (**Fig. 1** and **Methods**). With typical experimental pixel sizes (~100 nm), the dimensionality of the PSF images is moderate (modeled as 13×13 pixels), and thus artificial neural networks (ANN) with multiple hidden layers[21] were directly used as our learning model. ANN is beneficial here as it possesses excellent representational power; moreover, since ANN does not require domain-specific expertise to construct nonlinear models, it offers a facile means to train different target parameters in an end-to-end fashion.

65 One ANN with a final Softmax layer was first trained using cross-entropy loss to
66 determine the emitter color of each PSF. Once trained, the final Softmax output provided an
67 estimate for the conditional probability distribution of the fluorophore color, which enabled the
68 classification of each PSF image with known confidence (**Fig. 1a** and **Methods)**. For this color-
69 separating ANN, training data for different fluorophores were separately prepared from multiple
70 imaging sessions performed under the same experimental conditions as the final sample, but
71 using only one known fluorophore at a time. The training data contained sufficient samples for
72 fluorophores at different axial positions within the depth of field (~±500 nm of the focal plane),
73 so that the ANN was trained to recognize fluorophores for all axial positions.

74 In parallel, ANNs for resolving the axial position of the emitter were separately trained
75 for each fluorophore using L2 loss so that the final output was a scalar value[22] corresponding to
76 the decoded axial position (**Fig. 1b**). Training data for these axial-localization ANNs were
77 collected by step-scanning samples each containing one specific fluorophore, as is typically
78 performed for the calibration in existing 3D SMLM methods[9].

79 Once both trainings were completed, SMLM data from unknown samples were localized
80 in 2D, and the single-molecule images were first fed into the above color-separating ANN (**Fig.**
81 **1c**). The resultant, color-separated single-molecule images were then separately fed into the
82 above axial-localization ANNs trained with the corresponding fluorophores (**Fig. 1c**).
83 Multidimensional SMLM data were thus obtained by integrating the ANN-inferred color and
84 axial information with the initial 2D-localization results.

85 We first examined the performance of the color-separating ANN using two types of 40-
86 nm dia. fluorescent beads that differed by 45 nm in emission wavelength ("yellow" and

87 “orange”). When the beads are at the focal plane, fitting to simple Gaussian models yielded PSF
88 sizes ($2\sigma$) that were directly proportional to the emission wavelength (**Fig. 2a**), as expected. At
89 photon counts of 3000-4000, this difference gave adequate separation of the two colors (**Fig. 2a**).
90 However, this separation quickly fell apart when results from different axial positions were
91 mixed: unsurprisingly, defocusing led to substantially increased PSF sizes, and so this parameter
92 no longer offers useable color separation (**Fig. 2b**).

93 In contrast, our color-separating ANN recognized the nuances in the PSF patterns due to
94 differences in color vs. differences in axial position, and thus offered excellent color separation
95 both in the presence and absence of defocusing (**Fig. 2cd**). As mentioned, the output of this ANN
96 gives the conditional probabilities of each given single-molecule image being classified as
97 certain types of fluorophores. In the binary yellow-orange system, the results can be simplified
98 as the difference $\Delta$ between the evaluated probabilities of being orange and being yellow for
99 every image (**Fig. 2cd**). Even in the presence of defocusing, simple classification based on $\Delta>0$
100 and $\Delta<0$ gave near-perfect (~99% accuracy) identification for both types of beads in the photon
101 count range of 3000-4000 (**Fig. 2ef**). Note in STORM experiments, an average of >5000 photons
102 is often obtainable for single molecules[9,23]. Reducing the photon count to the range of 1000-1500
103 photons led to modest decreases in accuracy to 94.9% and 89.1% for the yellow and orange
104 beads, respectively (**Fig. 2ef**). These results were improved to 97.9% and 93.1%, respectively,
105 by only keeping classifications with $|\Delta|$ above the confidence threshold of 0.8, at the expense of
106 rejecting 8.6% and 13.5% classifications for the yellow and orange beads, respectively (**Fig. 2e**).
107 Our ANN approach can thus be readily tuned for experiments that emphasize color-separation
108 accuracy vs. experiments that emphasize the retention of molecules.

109 We next tackled cell imaging (**Fig. 3**). The microtubules and mitochondria in adherent
110 COS-7 cells were respectively immunolabeled with two STORM dyes, CF568 and Alexa Fluor
111 647 (AF647). Both dyes were excited within the same STORM imaging session, and resultant
112 single-molecule fluorescence was collected in one single optical path after a multi-notch filter.
113 For training of the first, color-separating ANN, COS-7 cells singly-labeled by CF568 and AF647
114 for microtubules were STORM-imaged on the same setup, which naturally contained single
115 molecules at all possible axial positions within the depth of field. For training of the second,
116 axial-localization ANN, dye-labeled antibodies were attached to the coverslip for step-scanning
117 in the axial direction (**Methods**).

118 **Figure 3a** presents the acquired STORM image colored by the fitted Gaussian width ($2\sigma$)
119 of the PSF of each molecule. Whereas it is clear that all the narrowest widths belonged to
120 microtubules, which were stained by the shorter-wavelength dye CF568, larger widths were
121 found at both microtubules and mitochondria (e.g., cyan arrows in **Fig. 3a**). This result is similar
122 to what we saw in the bead data (**Fig. 2b**): defocusing broadens the PSF width, and so this
123 simple parameter can no longer be used to separate colors. Remarkably, our color-separating
124 ANN achieved excellent color separation for the entire image independent of axial position (and
125 thus defocusing) (**Fig. 3b-d**), and consistent results were obtained on different cells over
126 repeated experiments (**Supplementary Fig. 1**). Quantification of color classification accuracy, as
127 separately determined using fixed cells singly labeled by CF568 (**Fig. 3f**) and AF647 (**Fig. 3g**),
128 indicated that at ~5000 photons, excellent accuracies of 98.2% were achieved for both dyes at
129 the confidence threshold of 0.8. At ~3000 photons, the accuracy for CF568 did not vary
130 noticeably (**Fig. 3f**), whereas the accuracy for AF647 dropped to ~90.4% (**Fig. 3g**). Lowering the
131 confidence thresholds led to accuracy drops by a few percentage points (**Fig. 3fg**). Previous

132 work[23] has shown that for dyes in these two color channels, through traditional sequential
133 imaging using different optical filter sets, a ~8% crosstalk occurred from the 561-nm excited dye
134 into the 647-nm excited dye, whereas crosstalk in the opposite direction was ~1%. Our
135 accuracies thus appear to outperform at ~5000 photons, a value often obtained in STORM
136 experiments[9,23]. Moreover, in our case, all data were collected within the same optical path in a
137 single STORM session, so we avoided the major difficulties in aligning images from different
138 filter sets.

139 Based on our successful color classification, two axial-localization ANNs, each trained
140 for AF647 and CF568, were next used to separately decode the axial positions of the molecules
141 in the two color channels, the results of which were recombined into one image for presentation
142 (**Fig. 3e** and **Supplementary Fig. 1**). This showed the expected result that the cell edges, thinner
143 in height, were dominated by small z values, whereas for regions far away for the cell edges, the
144 cells became thicker and had increased z values. White arrows in **Fig. 3ae** further point to
145 regions of microtubules, labeled by the same CF568 dye, where similarly increased PSF widths
146 were noted, but the ANN correctly identified one being below the focal plane whereas the other
147 above. We further note that as the two color channels are successfully separated, they may also
148 be separately fed into other recent methods that extract axial positions from unmodified
149 PSFs[17,18].

150 As a final note, our end-to-end framework is further characterized by exceptional speed.
151 Once trained, evaluation speeds were $>3.3\times10^5$ molecules/s (GPU acceleration) for both the
152 color-separating and the axial-localization ANNs. These speeds surpass traditional "fitting"
153 approaches[18], and so could be especially beneficial for speed-demanding applications including
154 online analysis.

Our finding highlights the rich, multidimensional information concealed in the details of the diffraction-limited image of a fluorophore, which was uniquely unleashed in this work through state-of-the-art machine learning algorithms. Not having to modify the PSF shape or divide single-molecule fluorescence between different optical paths, or to image sequentially, not only simplify experimental implementation, but more importantly, preclude the deterioration in SMLM performance due to enlarged PSFs and/or split channels, as well as the need to align localizations from different channels. Meanwhile, we note that our approach is not limited to a particular type of PSF or machine-learning algorithm. The co-evolution of our data-driven end-to-end framework with the ongoing efforts on PSF engineering[8] should thus lead to new improvements, and conceivably, fundamentally new types of imaging modalities, for multidimensional SMLM.

## Figures

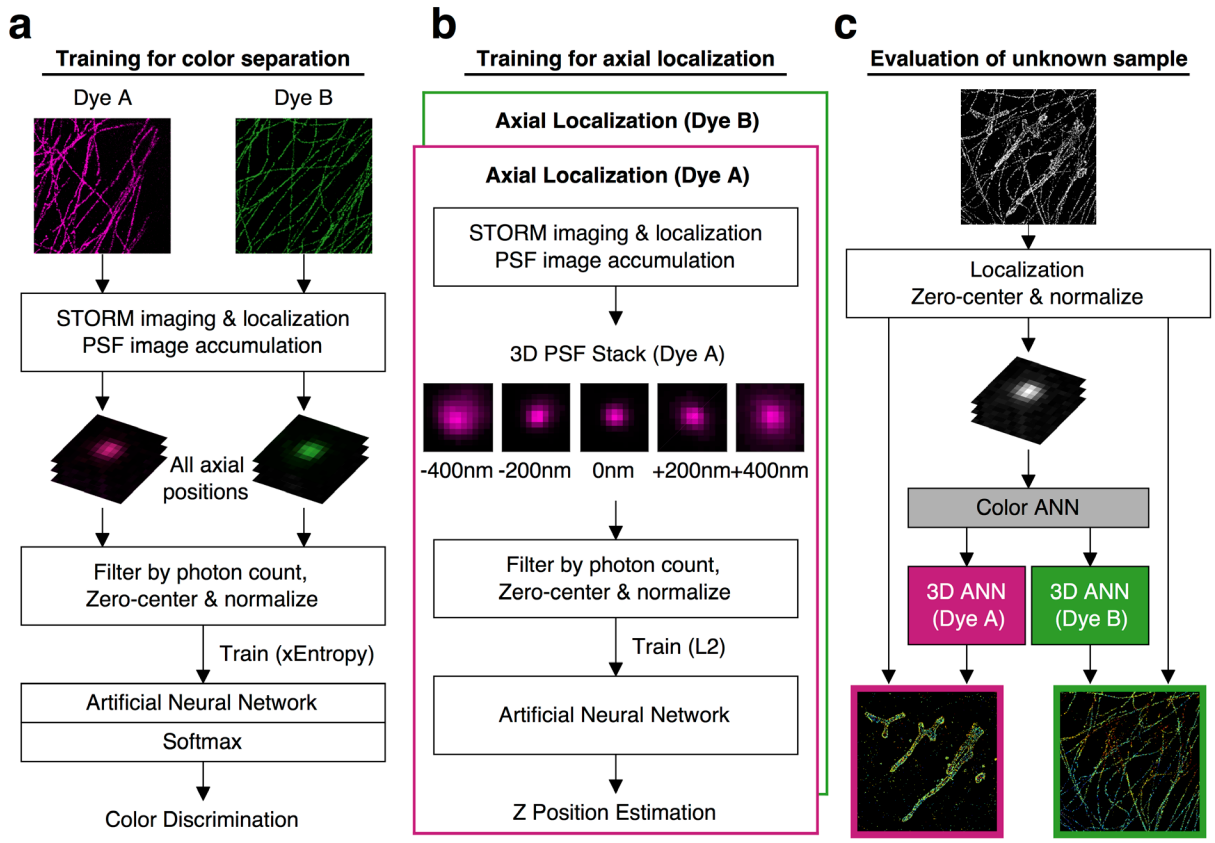


**Fig. 1 | Workflow of the machine learning-based multidimensional SMLM. (a)** A color-separating ANN is trained using samples each singly labeled by one known fluorophore, in which PSFs at different axial positions are well-represented. **(b)** ANNs for resolving the axial position are separately trained for each fluorophore using PSFs of known axial positions. **(c)** For the analysis of unknown samples, single-molecule images are localized in 2D, and first fed into the color-separating ANN described in (**a**). The color-separated single-molecule images are then separately fed into the axial-localization ANNs trained with the corresponding fluorophores, as described in (**b**). The resultant color and axial position information is then combined with the 2D localization of each molecule to generate the final multidimensional SMLM data.

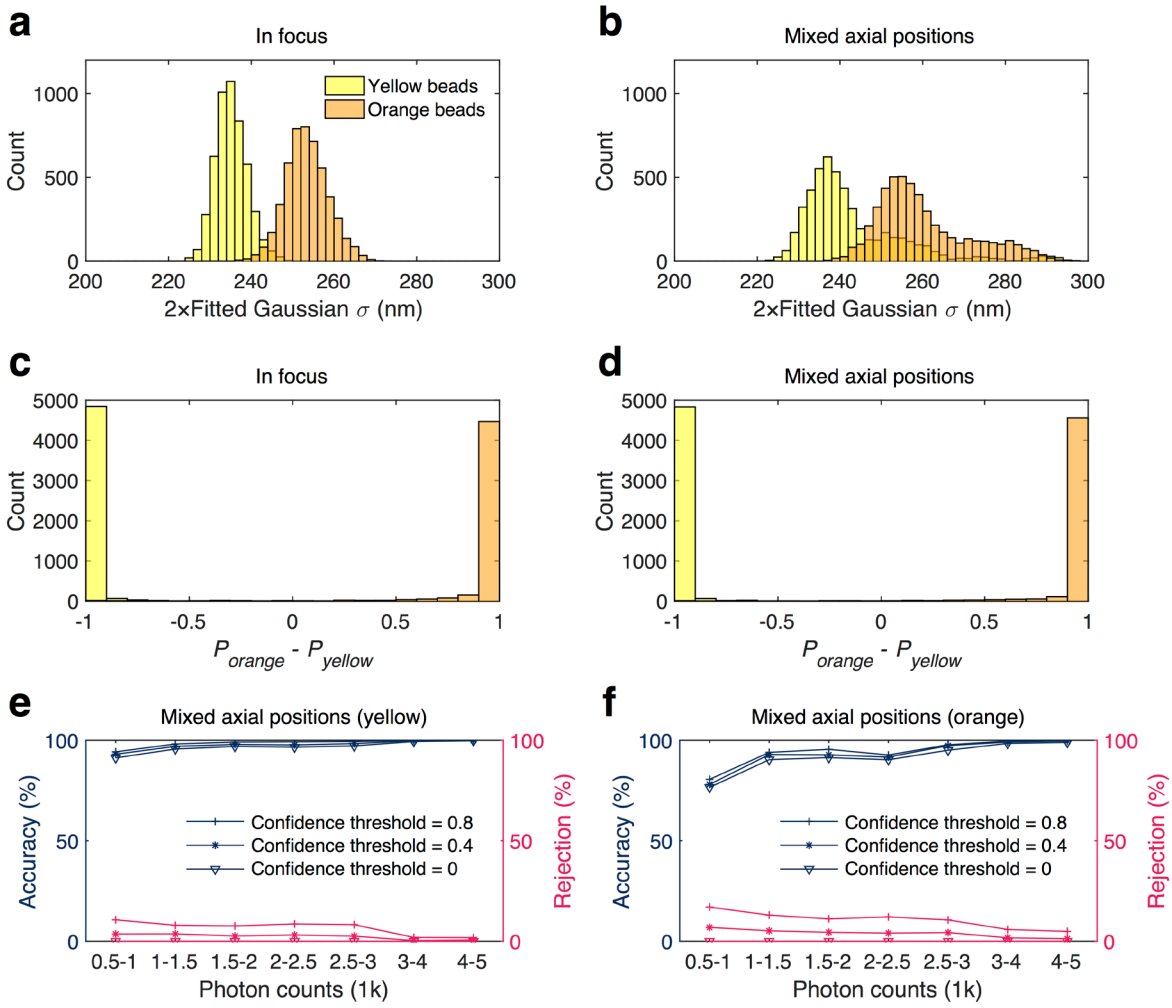


**Fig. 2 | Performance of the color-separating ANN for fluorescent beads.** (**a-b**) PSF size (2σ of 2D Gaussian fitting) distribution of "yellow" and "orange" beads emitting 3000-4000 photons, for (**a**) all beads are right at the focal plane and (**b**) the focus is evenly scanned over ±200 nm of the focal center. (**c-d**) Outputs of our color-separating ANN on the same datasets, presented as the distribution for the differences in the evaluated probabilities of each bead being "orange" vs. being "yellow". (**e-f**) Accuracy of classification (left axes) and rejection rate (right axes) as a function of photon count for the "yellow" (**e**) and "orange" (**f**) beads in the presence of defocusing, for confidence thresholds of 0, 0.4, and 0.8.

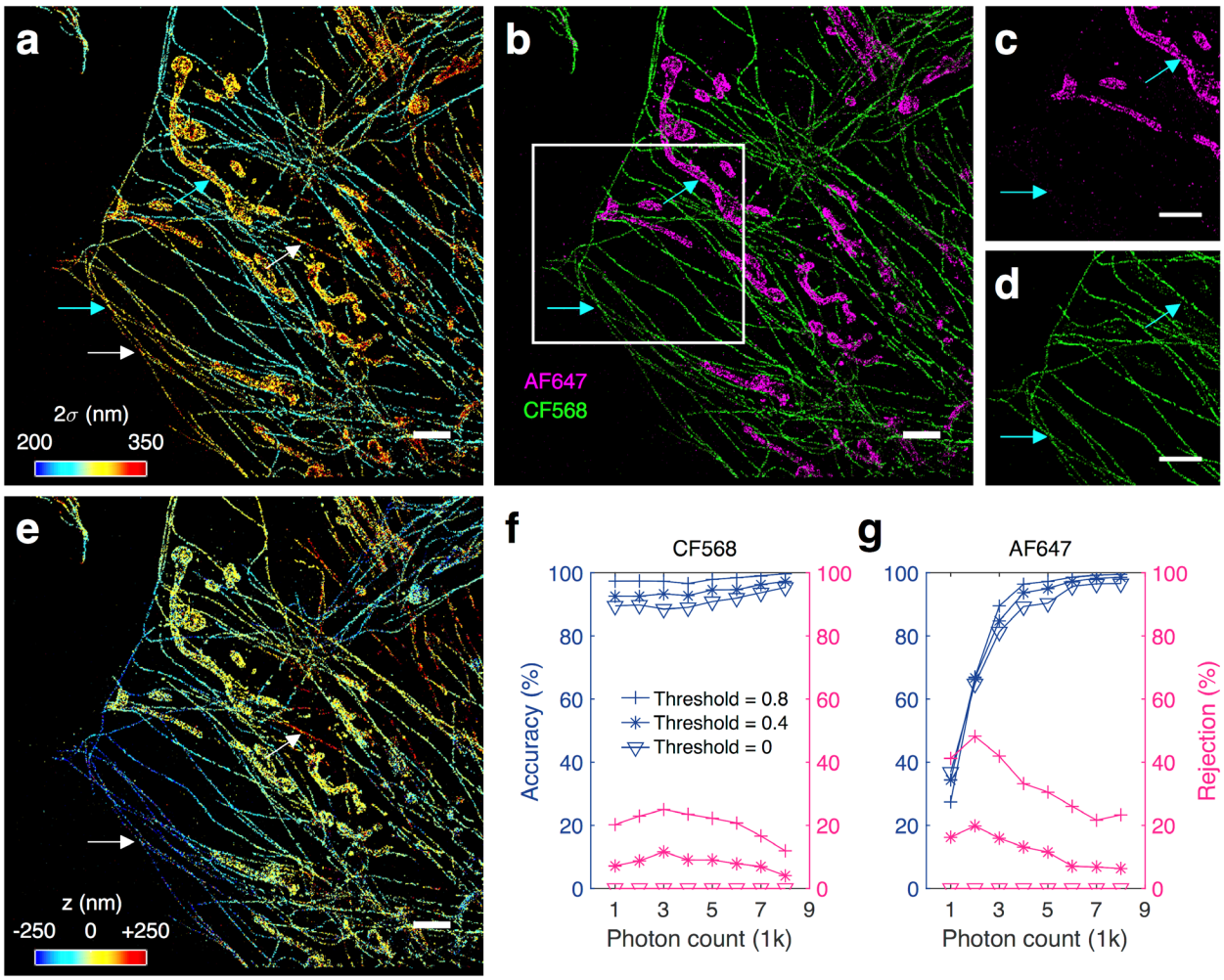


**Fig. 3 | ANN-resolved multicolor 3D SMLM in cells based on unmodified PSFs.** (**a**) STORM image of CF568-labeled microtubules and AF647-labeled mitochondria in a fixed COS-7 cell, colored by the fitted Gaussian width (2σ) of the PSF of each molecule, for molecules brighter than 3,000 photons. **(b)** Result of the color-separating ANN for the same dataset, at a confidence threshold of 0.8. (**c-d**) The separated AF647 (**c**) and CF568 (**d**) channels for the boxed area in (**b**). Cyan arrows in (**a-d**) point to two regions where molecules of similar PSF widths are correctly determined as different colors by the ANN. **(e)** The merged 3D STORM image after separately determining the axial position of every single molecule based on ANNs respectively trained for AF647 and CF568. Color here presents the axial position (*z*), with blue being closest to the substrate and red being the farthest away. White arrows in (**a**) and (**e**) point to two regions of the CF568 microtubule labeling that showed similar defocusing effects, but determined by ANN as being on opposite sides of the focal plane. Scale bars, 2 μm (**a-e**). **(f-g)** Classification accuracy (left axis) and rejection rate (right axis) of the color-separating ANN as a function of photon count, for cells singly labeled by CF568 (**f**) and AF647 (**g**), at confidence thresholds of 0, 0.4, and 0.8.

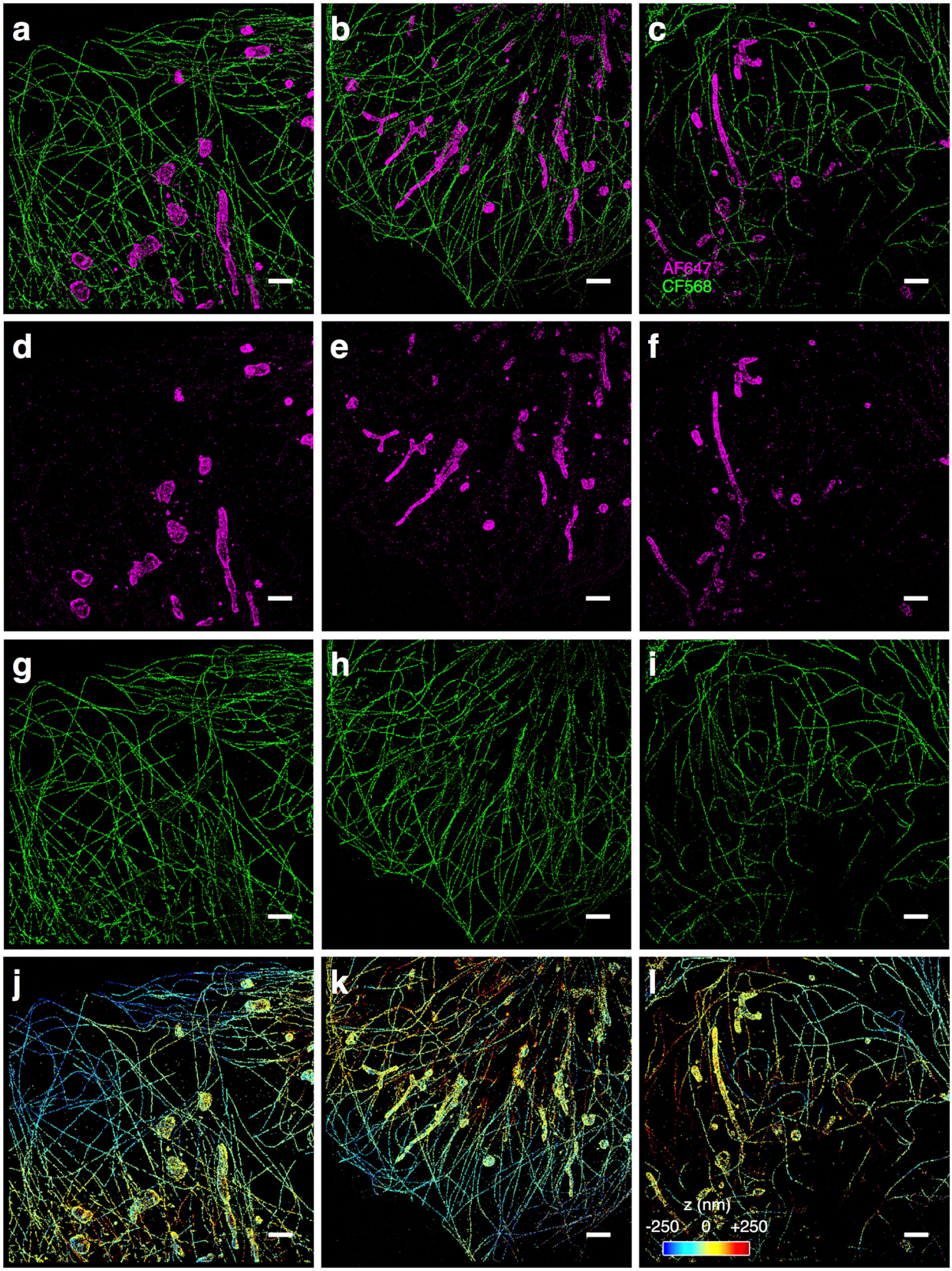


**Supplementary Fig. 1.** Additional examples of ANN-resolved multicolor 3D SMLM of fixed cells based on unmodified PSFs. Scale bars, 2 μm.

206 **Methods**

207 **Optical setup.** STORM and bead experiments were performed on a Nikon Ti-E inverted
208 fluorescence microscope using an oil-immersion objective lens (Nikon CFI Plan Apochromat λ
209 100×, NA 1.45) and the native 1.5x magnification on the microscope, without any modifications
210 to the imaging path. Lasers emitting at 644, 561, and 488 nm were introduced to the back focal
211 plane of the objective lens via a multi-line dichroic mirror (ZT405/488/561/640rpc-uf2,
212 Chroma). A translation stage shifted the laser beams toward the edge of the objective lens so that
213 they entered slightly below the critical angle, illuminating <1 μm into the sample. Emission was
214 filtered by a multi-notch filter (ZET405/488/561/640m, Chroma) and recorded by an EM-CCD
215 camera (iXon Ultra 897, Andor). Effective magnification and pixel size were ~150x and ~107
216 nm, respectively.

217 **Bead samples.** 40 nm dia. fluorescent beads from Invitrogen (F10720; "yellow" and "orange"
218 FluoSpheres with emission peaks at 515 and 560 nm, respectively) were diluted in Dulbecco's
219 phosphate buffered saline (DPBS), mixed, and sealed between a glass slide and a pre-cleaned
220 #1.5 thickness coverslip, and imaged with the above optical setup. The 488-nm and 561-nm
221 lasers were used to excite the two types of beads to similar levels of brightness. To record
222 images at different axial positions, the objective lens was scanned by the built-in motor over a
223 range of −200 to +200 nm of the focal plane.

224 **Cell samples.** COS-7 cells were plated on #1.5 coverslips to reach a confluency of ~50% in ~1.5
225 days, and fixed with 0.1% glutaraldehyde and 3% paraformaldehyde in DPBS at room
226 temperature. The sample was quenched with 0.1% sodium borohydride in DPBS and rinsed with
227 DBPS three times. Primary and secondary antibodies were diluted in a blocking buffer (3% BSA
228 + 0.1% Triton X-100 in DPBS) and labeled as described previously[9]. Primary antibodies were

229 mouse anti-tubulin (Abcam ab7291) for microtubules and rabbit anti-Tom20 (Santa Cruz sc-
230 11415) for mitochondria. Secondary antibodies were AF647-labeled goat anti-mouse IgG1
231 (Invitrogen A21240), AF647-labeled goat anti-rabbit IgG (Invitrogen A21245), and donkey anti-
232 mouse IgG (Jackson ImmunoResearch) conjugated with a CF568 succinimidyl ester (Biotium
233 92131). Samples for training the color-separating ANN were singly labeled for microtubules
234 with CF568 or AF647, whereas for the two-color unknown samples, microtubules and
235 mitochondria were respectively labeled with CF568 and AF647. The sample was mounted in a
236 STORM buffer [10% (w/v) glucose, 120 mM cysteamine, 0.8 mg/mL glucose oxidase, and 40
237 μg/mL catalase in Tris-HCl (pH 7.5)] and imaged using the optical setup described above. For
238 consistent experimental conditions, all cell samples were imaged at comparable depths with the
239 focal plane being ~300 nm away from the coverslip surface. The sample was illuminated with
240 the 561 and 644 nm lasers at ~2 kW/cm$^2$, which led to the photoswitching of CF568 and AF647
241 single molecules. Fluorescence was recorded by the EM-CCD for a frame size of 256x256 pixels
242 at 55 frames per second. Each movie was typically recorded for 20,000 frames.

243 **Antibody samples.** Training data for the axial localization of AF647 and CF568 single
244 molecules were acquired using the above AF647- and CF568-labeled secondary antibodies. The
245 two antibodies were separately diluted in DPBS to ~2 μg/mL. Pre-cleaned #1.5 coverslips were
246 separately incubated in either solution for ~5 min, briefly air-dried, rinsed with distilled water,
247 and mounted and imaged as described above. To record single-molecule images at different axial
248 positions, the objective lens was scanned by the built-in motor in the range of −700 to +700 nm
249 of the focal plane.

250 **Preprocessing of single-molecule images for ANNs.** Single-molecule fluorescence in raw
251 STORM and bead data was first identified and localized in 2D using established methods[1].

Single-molecule PSF images were cropped as 13x13 pixels surrounding the 2D localizations; at this time, images containing multiple emitting molecules were rejected. The cropped PSF images were zero-centered, and their L2/Euclidean norm was normalized before being used as inputs for ANNs.

**Design and implementation of neural networks.** An ANN architecture comprising multiple hidden layers was implemented using the Tensorflow framework on a computer with 32GB RAM, Intel i7-7800X CPU, and Nvidia GTX-1080Ti GPU. The same architecture was used for both the color-separating and axial-localization ANNs (4 total layers of 4096-4096-2048-1024 neurons, respectively). Each hidden layer was fully connected, and rectified linear units were used as their activation function. For color discrimination, Softmax function and cross-entropy were used for loss calculation, the weights in the network were not directly included for regularization, and a dropout layer was inserted before the final layer to prevent over-fitting. For axial localization, the output of the final layer was set to be a scalar value, and L2 norm was used to calculate the learning loss for each batch. In this case, L2 norm of the weights in each layer was added to the loss function for regularization, and dropout was not used. Network hyper-parameters such as the number of neurons in each layer (given above), the dropout ratio (0.5 for the color-separating ANN), and the regularization factor (0.01 for the axial-localization ANNs) were adjusted for optimized performance.

**Neural network training.** Since the network is subject to handling input images with various noise levels, it was essential to maintain a consistent noise level within the training dataset regardless of the classification class or axial location. Therefore, experimental PSF images with comparable photon counts of 4500-5500 were used throughout the training process, and molecules with photon counts higher than this range were used for the validation during the

training process to check the generalization of the trained network. The weights initialized by the Xavier method[24] are trained using the Adam optimization algorithm. An initial learning rate of $10^{-4}$ and $10^{-3}$, and a batch size of 64 and 32 were used for the color-separating and the axial-localization ANNs, respectively. The learning rate was set to decrease by ~5x after every 1,000 iterations. The sizes of the training sets were ~10,000 and ~6,000 per fluorophore type for the color-separating and the axial-localization ANNs, respectively. The networks converged within ~10 epochs (training time: 231.9 s for the color-separating ANN, and 488.5 s for the axial-localization ANNs).

**Neural network inference.** At the inference stage, input single-molecule PSF images were first plugged into the color-separating ANN. This ANN provides a conditional probability distribution corresponding to the input image. Specifically, when the size of each input image is $N$ by $N$ pixels, and there are $M$ different molecule color classes, the final output from the Softmax layer for the $i$th input image is

$$P(y_i|x_i),\ x_i \in \mathbb{R}^{N\times N},\ y_i \in \{\text{Dye 1}, \cdots, \text{Dye M}\}. \tag{1}$$

From this distribution, the ANN makes the decision in a maximum-likelihood manner: the molecule color class with the highest probability is chosen. This, in turn, implies that we can use this distribution to quantify the classification confidence. For example, in a simple binary classification problem, the confidence for the color assignment of the $i$th input image can be evaluated as

$$|\Delta_i| = |P(\text{Dye 1}|x_i) - P(\text{Dye 2}|x_i)|. \tag{2}$$

By setting a finite confidence threshold $\delta$ to reject molecules with low classification confidences ($|\Delta_i|<\delta$), improved classification accuracy may be obtained (**Figs. 2ef** and **3fg**). This parameter

may thus be adjusted by the user to balance the classification accuracy and rejection rate. Once the color of the molecule is determined, the single-molecule image is plugged into the axial-localization ANN trained for that particular color to evaluate the axial position. With GPU acceleration, both inference steps (passing the forward path of the neural networks) were extremely fast: only ~300 ms was used to infer 100,000 molecules for both the color-separating and the axial-localization ANNs.

## Acknowledgments

This work was in part supported by the Beckman Young Investigator Program and the Packard Fellowships for Science and Engineering. K.X. is a Chan Zuckerberg Biohub investigator. T.K. acknowledges support from Kwanjeong Educational Foundation. S.M. acknowledges support from Samsung Scholarship.

## References

1. Rust, M. J., Bates, M. & Zhuang, X. Sub-diffraction-limit imaging by stochastic optical reconstruction microscopy (STORM). *Nat. Methods* **3,** 793–796 (2006).
2. Betzig, E. *et al.* Imaging intracellular fluorescent proteins at nanometer resolution. *Science* **313,** 1642–1645 (2006).
3. Hess, S. T., Girirajan, T. P. K. & Mason, M. D. Ultra-high resolution imaging by fluorescence photoactivation localization microscopy. *Biophys. J.* **91,** 4258–4272 (2006).
4. Sharonov, A. & Hochstrasser, R. M. Wide-field subdiffraction imaging by accumulated binding of diffusing probes. *Proc. Natl. Acad. Sci.* **103,** 18911–18916 (2006).

319 5. Yan, R., Moon, S., Kenny, S. J. & Xu, K. Spectrally resolved and functional super-resolution
320 microscopy via ultrahigh-throughput single-molecule spectroscopy. *Acc. Chem. Res.* **51,** 697–705
321 (2018).
322 6. Moon, S. *et al.* Spectrally resolved, functional super-resolution microscopy reveals nanoscale
323 compositional heterogeneity in live-cell membranes. *J. Am. Chem. Soc.* **139,** 10944–10947 (2017).
324 7. Backlund, M. P., Lew, M. D., Backer, A. S., Sahl, S. J. & Moerner, W. E. The role of molecular
325 dipole orientation in single-molecule fluorescence microscopy and implications for super-
326 resolution imaging. *ChemPhysChem* **15,** 587–599 (2014).
327 8. von Diezmann, A., Shechtman, Y. & Moerner, W. E. Three-dimensional localization of single
328 molecules for super-resolution imaging and single-particle tracking. *Chem. Rev.* **117,** 7244–7275
329 (2017).
330 9. Huang, B., Wang, W., Bates, M. & Zhuang, X. Three-dimensional super-resolution imaging by
331 stochastic optical reconstruction microscopy. *Science* **319,** 810–813 (2008).
332 10. Shtengel, G. *et al.* Interferometric fluorescent super-resolution microscopy resolves 3D cellular
333 ultrastructure. *Proc. Natl. Acad. Sci.* **106,** 3125–3130 (2009).
334 11. Bossi, M. *et al.* Multicolor far-field fluorescence nanoscopy through isolated detection of distinct
335 molecular species. *Nano Lett.* **8,** 2463–2468 (2008).
336 12. Zhang, Z., Kenny, S. J., Hauser, M., Li, W. & Xu, K. Ultrahigh-throughput single-molecule
337 spectroscopy and spectrally resolved super-resolution microscopy. *Nat. Methods* **12,** 935–938
338 (2015).
339 13. Pavani, S. R. P. *et al.* Three-dimensional, single-molecule fluorescence imaging beyond the
340 diffraction limit by using a double-helix point spread function. *Proc. Natl. Acad. Sci.* **106,** 2995–
341 2999 (2009).
342 14. Shechtman, Y., Weiss, L. E., Backer, A. S., Lee, M. Y. & Moerner, W. E. Multicolour localization
343 microscopy by point-spread-function engineering. *Nat. Photonics* **10,** 590–594 (2016).

15. Smith, C., Huisman, M., Siemons, M., Grünwald, D. & Stallinga, S. Simultaneous measurement of emission color and 3D position of single molecules. *Opt. Express* **24,** 4996 (2016).

16. Siemons, M., Hulleman, C. N., Thorsen, R. Ø., Smith, C. S. & Stallinga, S. High precision wavefront control in point spread function engineering for single emitter localization. *Opt. Express* **26,** 8397–8416 (2018).

17. Franke, C., Sauer, M. & van de Linde, S. Photometry unlocks 3D information from 2D localization microscopy data. *Nat. Methods* **14,** 41–44 (2016).

18. Li, Y. *et al.* Real-time 3D single-molecule localization using experimental point spread functions. *Nat. Methods* **15,** 367–369 (2018).

19. Gibson, S. F. & Lanni, F. Diffraction by a circular aperture as a model for three-dimensional optical microscopy. *J. Opt. Soc. Am. A* **6,** 1357 (1989).

20. Kuntzer, T., Tewes, M. & Courbin, F. Stellar classification from single-band imaging using machine learning. *Astron. Astrophys.* **591,** A54 (2016).

21. Bishop, C. M. *Neural networks for pattern recognition*. (Oxford University Press, Inc., 1995).

22. Hara, K., Vemulapalli, R. & Chellappa, R. Designing deep convolutional neural networks for continuous object orientation estimation. *ArXiv170201499 Cs* (2017).

23. Dempsey, G. T., Vaughan, J. C., Chen, K. H., Bates, M. & Zhuang, X. Evaluation of fluorophores for optimal performance in localization-based super-resolution imaging. *Nat. Methods* **8,** 1027–1036 (2011).

24. Glorot, X. & Bengio, Y. Understanding the difficulty of training deep feedforward neural networks. in *Proceedings of the Thirteenth International Conference on Artificial Intelligence and Statistics* 249–256 (2010).